Soft Matter

Rheology of bi-disperse dense fiber suspensions

Journal:	*Soft Matter*
Manuscript ID	SM-ART-06-2023-000787.R1
Article Type:	Paper
Date Submitted by the Author:	02-Nov-2023
Complete List of Authors:	Khan, Md Monsurul Islam; Purdue University, Mchanical Engineering Corder, Ria; Purdue University, Mechanical Engineering Erk, Kendra; Purdue University, Materials Engineering Ardekani, Arezoo; Purdue University System,

Rheology of bi-disperse dense fiber suspensions

Monsurul Khan,[1] Ria D. Corder,[1] Kendra A Erk,[2] and Arezoo M. Ardekani[1]

[1]*School of Mechanical Engineering, Purdue University, West Lafayette, Indiana 47907, USA*
[2]*School of Materials Engineering, Purdue University, West Lafayette, Indiana 47907 USA*

(Dated: November 18, 2023)

While significant progress has been made in the modeling and simulation of uniform fiber suspensions, no existing model has been validated for industrially-relevant concentrated suspensions containing fibers of multiple aspect ratios. In the present work, we investigate bi-disperse suspensions having two fiber populations of varying aspect ratio in a steady shear flow using direct numerical simulations. Moreover, we measure the suspension viscosity by creating a controlled length bidispersity for nylon fibers suspended in a Newtonian fluid. The results showed a good agreement between experimental and numerically predicted viscosity for bi-disperse suspension. The ratio between the aspect ratio of large to small fibers (size ratio) and the volume fraction of large fibers (composition) in bi-disperse systems strongly affected the rheological behavior of the suspension. The increment of relative viscosity associated with size ratio and composition can be explained by the decrease in the maximum flowable limit or jamming volume fraction. Moreover, the relative viscosity of bi-disperse suspensions collapse, when plotted against reduced volume fraction ϕ/ϕ_m, demonstrating the controlling influence of the jamming fraction in bi-disperse fiber suspensions.

I. INTRODUCTION

Fiber suspensions are widely encountered in the production of material and consumer goods, chemical processing, and the extraction of natural resources [1–3]. Furthermore, fibers are mixed with concrete to strengthen and alter its performance [4], the rheological properties of drilling fluids are adjusted by adding such fibers [5], and the paper making process from wood fibers is highly dependent on the fluid mechanics [3]. In these examples, we encounter conditions with high solid contents, and the materials are frequently referred to as dense or concentrated suspensions. The viscosity increases and even diverges as the solid contents approach the jamming volume fraction (ϕ_m) at which the system is presumed to jam and fluidity ceases [6, 7]. Consequently, the power requirements for pumping and mixing increase significantly, leading to an increase in the processing cost. Therefore, understanding the rheological properties of these fiber suspensions is critical for comprehending and manipulating flow behavior in order to ensure optimal performance [8–10]. However, such suspensions are challenging to study due to many degrees of freedom of the fiber deformation and microscopic instabilities [11]. Moreover, the rheological properties of these suspensions are complex and heavily dependent on several variables, including suspending fluid properties, fiber size distribution, shape, flexibility, roughness, and volume fractions [12–21]. Even though fiber size distributions are more commonly encountered in the applications and natural environments stated above than mono-disperse suspensions, the role of bi- or poly-dispersity on the rheology of fiber suspensions is limited in the literature.

The relative viscosity of mono-disperse dilute fiber suspensions have been understood showing qualitative agreement between theoretical predictions considering pure hydrodynamics interactions [22, 23] and experimental studies [24]. However, as the concentration increases, the non-hydrodynamic contribution (such as frictional contact) appears, and the theoretical predictions considering pure hydrodynamics interactions do not hold in semi-dilute and concentrated suspensions [25, 26]. Recently, we have developed a numerical model by incorporating short-range interactions via attractive and repulsive interactions and contact interactions in the dense fiber suspension [12–14, 27]. The model presented in this study effectively describes the rheological characteristics of dense fiber suspensions as found in experimental settings [19, 20]. These characteristics include the existence of a yield stress, shear thinning rheology, and normal stress differences. In all of the aforementioned investigations, the fibers under consideration exhibit uniform size characteristics, hence enabling the development of a fiber suspension model that does not incorporate the complexities associated with fiber size distribution. Nevertheless, it is widely acknowledged that the majority of systems exhibit inherent non-uniformity in terms of size, hence emphasizing the necessity for a comprehensive understanding of non-uniform suspensions from a physical standpoint [28].

Efforts to comprehend the effect of polydispersity have been initiated by Marrucci and Grizzuti [29, 30] by extending the Doi and Edwards [31, 32] theory of mono-disperse suspensions to bi-disperse suspensions. According to Marrucci and Grizzuti [29, 30], the zero-shear viscosity and shear thinning of fibers are length dependent, with longer fibers having a higher zero shear viscosity than smaller ones but achieving better orientation ordering than shorter ones, resulting in more pronounced shear thinning behavior. Furthermore, they assume that in the low shear rate regime, the short fibers dominate over the long ones, while at high shear rates, the longer fibers aid in the orientational ordering of the short species. However, their assumption has been refuted by Larson and Mead [33], who demonstrated that the

dynamics of both fiber species in the quasi-linear deformation regime are equally significant because the longer species slows the rotation of the shorter species, whereas the presence of the shorter species enables the longer species to rotate relatively faster. The dependence of the rheology on the bi-dispersity has been predominantly investigated in dense suspensions of spherical particles [34, 35]. However, the impact of bi-dispersity on rheology in fiber suspensions has not been thoroughly examined, which is the main objective of this research. Nevertheless, the factor imposing difficulty on the study of bi-dispersity on fiber suspension is that making precise bi-disperse suspensions can be experimentally challenging. In this work, we develop an experimental setup to perform rheology measurements at a controlled length bi-dispersity of the fibers. While experimental measurements play a crucial role in comprehending the fundamental mechanisms of bi-disperse suspensions, they have certain limitations. For instance, the measurement of fiber shape and orientation poses challenges. The direct numerical simulations conducted in this study will provide additional insights to the experimental methods employed in comprehending the rheology of bi-disperse fiber suspensions.

The transportation of suspensions with high solid volume fractions is a critical in the optimization of processes and the enhancement of efficiency across several industrial applications. Nevertheless, in the case of high solid fractions, frictional fiber flows can give rise to the formation of enduring, dense, and system-spanning force chains that exhibit significant resistance against the flow. Jamming occurs when the solid volume fraction reaches a critical point at which the viscosity becomes infinitely high, resulting in the suspension becoming immobile regardless of the magnitude of the applied shear force [7, 36]. Empirical evidence indicates that there is an inverse relationship between the volume fraction of jamming and the length of the fiber in experiments [6]. The dependence of jamming on the fibers' surface roughness and aspect ratio ($A = L/D$, where L is the length and D is the diameter of the fiber) has been quantified in our previous publications on mono-disperse fiber suspensions [13, 14]. The decrease in relative viscosity is a widely recognized phenomenon when the length of the longer fiber grows, hence highlighting the need of studying the jamming volume fraction in bi-disperse solutions. Nevertheless, the impact of bidispersity on the jamming volume percentage has solely been examined in the context of suspensions consisting of spherical particles with two distinct sizes. Hence, we aim to evaluate the impact of bi-dispersity on the jamming volume percentage in suspensions of fibers.

In this work, we comprehensively study the effect of bi-dispersity on the rheology of fiber suspensions. The measurement is carried out by creating a controlled length bi-dispersity for nylon fibers suspended in a Newtonian fluid, maintaining the overall volume fraction constant. Moreover, we propose a numerical model to probe the role of bi-dispersity on suspension rheology in dense fiber suspensions and compare the results with the experimental measurements. Our proposed model incorporates short-range interactions via attractive and repulsive interactions and contact interactions that do a good job of quantitatively capturing experimentally observed shear thinning and bi-disperse rheology. In addition to reproducing experimentally observed trends, we gain an additional understanding of the variation of normal stress differences and jamming volume fraction with bi-dispersity. Moreover, we examine the microstructure of these bi-disperse suspensions via the orientation distribution of the fiber. To this end, we present the measurement procedure, experimental device, and details of fiber suspension in section II. In section III, we briefly discuss the governing equation, inter-fiber interactions, and simulation conditions, followed by results and a discussion of the effect of bi-dispersity on bulk rheological properties. Finally, we deduce the functional forms of the dependency of the jamming volume fraction on the controlling parameters, which may be utilized to optimize the transport and handling of dense fiber suspensions.

II. EXPERIMENT

In the present study, we investigate the bi-disperse suspension of nylon fibers. We discuss the characterization and suspension preparation in section II A and II B, while the measuring protocols will be briefly described in II C.

A. Materials

Short cut nylon fibers (industrial/textile grade polyamide, 20 denier, nominal lengths = 0.6 and 1.0 mm and nominal diameter = 49.8 μm , Engineered Fibers Technology) and glycerol (99+%, Thermo Scientific Chemicals) were used as received. Average fiber dimensions (length, diameter, and aspect ratio) were obtained using an Olympus BX41 microscope and ImageJ, are presented in Table I. The details of the measurements and distribution can be found in supplemental material (Figure S1).

TABLE I: Average lengths, diameters, and aspect ratios of the small and large nylon fibers used in this work. Data is presented as average values ±1 standard deviation.

Fiber type	Length (mm)	Diameter (mm)	Aspect Ratio (A)
Small (s)	0.659 ± 0.015	0.0501 ± 0.0047	13.3 ± 1.3
Large (l)	1.050 ± 0.070	0.0506 ± 0.0039	21.0 ± 2.2

B. Suspension preparation

The nylon fibers were suspended in a density-matched suspending medium composed of 54 v% glycerol, 46 v% deionized water (Figure S2 and details in the supplemental material). Based on the empirical formulas presented by Cheng [37] with adjustments proposed by Volk and Kähler [38] , we estimate the density-matched suspending medium and nylon fibers are of density ≈ 1.15 g/cm3 at 21 °C. Suspensions were prepared in 80 mL quantities by combining specified volume fractions of nylon fibers and suspending medium, and mixing overnight via magnetic stirring at room temperature, after which the suspensions were stored at room temperature prior to measurements.

C. Rheometry

Steady-shear rheometry experiments were performed at room temperature using an Anton Paar MCR 702 rheometer equipped with the Flexible Cup Accessory, 4-bladed vane (Anton Paar ST24-4V-30/24, diameter = 24 mm and blade length = 30 mm), and 100 mL PYREX beaker (diameter = 46.3 mm). The vane-in-cup geometry was calibrated using heavy mineral oil (Sigma Aldrich) to allow for quantitative viscosity values to be obtained using this relative measuring accessory [39]. This geometry does not allow for direct measurement of normal stresses or normal stress differences. During each experiment, 80 mL of suspension was added to the 100 mL PYREX beaker, and then the vane was lowered into the beaker (gap height = 1 mm). After allowing the sample to equilibrate for 15 min, increasing (shear rates 0.1–10s^{-1}) and decreasing (shear rates 10 – 0.1 s-1) flow sweep experiments were performed (20 points per decade, 20 s/pt for both ramps). Data are reported from the second (decreasing) flow sweep experiment. The viscosity of the suspending medium, η_0, was measured as 10.0 mPa s.

III. SIMULATION METHODOLOGY

In this section, we discuss the governing equations and numerical methods used to simulate the shear flow of the bi-disperse fiber suspension. We consider a suspension of total N fibers of two different aspect ratios (A_s and A_l) in a shear flow with top and bottom walls moving in opposite directions with an imposing shear rate $\dot{\gamma}$. We use the method and algorithm in Khan *et al.* [13], which we briefly discuss here.

A. Governing Equations

As the fibers are suspended in a fluid flow, the hydrodynamic forces acting on the fibers need to be related to their deformation to get their configuration in the flow. Thus, the elasticity equation of slender bodies is solved. We introduce the governing equations for fluid flow and motion of flexible fibers as follows.

1. Fluid flow equations

The suspended fluid is considered to be an incompressible Newtonian fluid with constant density, which is governed by continuity and Navier-Stokes equations.

$$\nabla \cdot \mathbf{u} = 0, \tag{1}$$

$$\frac{\partial \mathbf{u}}{\partial t} + \nabla \cdot (\mathbf{u} \otimes \mathbf{u}) = -\nabla p + \frac{1}{Re}\nabla^2 \mathbf{u} + \mathbf{f}. \tag{2}$$

where $\mathbf{u}$ is the velocity field, p is the pressure, $\mathbf{f}$ is the volume force arises due to presence of fibers, and $Re = \rho\dot{\gamma}{L_l}^2/\eta$ is the Reynolds number, where ρ is the density of the fluid, η is the dynamic viscosity of the suspending fluid, and L_l is the characteristic length scale which is also the length of the larger fiber in the bi-disperse suspension.

2. Fiber equations

In our current framework, we consider the fiber as neutrally buoyant and inextensible. The dynamics of thin flexible fiber can be described as Euler-Bernoulli equation [40].

$$\rho_l \frac{\partial^2 \mathbf{X}}{\partial t^2} = \frac{\partial}{\partial s}(T\frac{\partial \mathbf{X}}{\partial s}) - B\frac{\partial^4 \mathbf{X}}{\partial s^4}) + \rho_l \mathbf{g} - \mathbf{F} + \mathbf{F}^f, \tag{3}$$

where $\rho_l = (\rho_f - \rho)A_f$ is the linear density difference, ρ_f is the fiber linear density and A_f is their cross section. Moreover, $\mathbf{X} = (x(s,t), y(s,t), z(s,t))$ is the fiber position, s the curvilinear coordinate along the fiber, T is the tension, $B = EI$ is the bending rigidity with E the elastic modulus of the fiber and I the second moment of the area around the fiber axis, $\mathbf{g}$ the gravitational acceleration, $\mathbf{F}$ is the fluid-solid interaction force, $\mathbf{F}^f$ is the inter-fiber interaction forces. In general, fibers have the ability to both extend and bend, but usually, because of their high extensional resistance, it is assumed that they cannot extend and can only bend [41, 42]. The constraint of inextensibility is :

$$\frac{\partial \mathbf{X}}{\partial s}.\frac{\partial \mathbf{X}}{\partial s} = 1. \tag{4}$$

Equations 3 and 4 are made dimensionless by choosing larger fiber length L_l as reference length, a reference velocity U, and fiber linear density ρ_f as reference density. Therefore, the dimensionless bending rigidity is $B^* = \frac{B}{\rho_f \dot{\gamma}^2 {L_l}^4}$. Since the left-hand side (LHS) of equation 3 is zero, to avoid singularity in the coefficient matrix, we modify the dimensionless form of equation 3 as [42]

$$\frac{\partial^2 \mathbf{X}}{\partial t^2} = \frac{\partial^2 \mathbf{X}_{fluid}}{\partial t^2} + \frac{\partial}{\partial s}(T\frac{\partial \mathbf{X}}{\partial s}) - B\frac{\partial^4 \mathbf{X}}{\partial s^4} - \mathbf{F} + \mathbf{F}^f, \tag{5}$$

where the first term in right-hand side (RHS) is the fluid particle acceleration which is identical to left-hand side (LHS) for neutrally buoyant fibers. As the fibers are suspended in the fluid medium, we impose zero force, moment, and tension at the free ends.

$$\frac{\partial^2 \mathbf{X}}{\partial s^2} = 0, \frac{\partial^3 \mathbf{X}}{\partial s^3} = 0, T = 0 \tag{6}$$

B. Numerical method

Nonlinear sets of equations, as described above, control the problems and necessitate effective numerical methods. The motion of the fluid and the solid should be correctly coupled since the fibers interact with the fluid flow. Additionally, the computationally intensive short-range interactions between the fibers should be taken into account.

The fluid equations are solved using [43] on a uniform staggered grid. The time integration is based on the classical method of projection [44]. The central difference scheme is utilized to spatially discretize convective and diffusive terms, whereas the Adams-Bashforth scheme is utilized to temporally integrate convective terms. [17]. In order to determine the position of the fibers, the Euler-Bernoulli equations are solved alongside the tension equation. The tension equation is coupled with the Euler-Bernoulli equations, and solving both simultaneously necessitates solving nonlinear sets of equations, resulting in a long computation time. Huang *et al.* [41] proposed an effective two-step procedure to circumvent these complications. In this method, all equations are discretized using the finite difference method on a staggered grid, and then a predicted value for fiber position is computed using the previous time steps. The details of the two-step method for solving Euler-Bernoulli equations can be found elsewhere [17].

Finally, to couple the fluid and the solid motion, the immersed boundary method (IBM) is utilized. In this approach, two sets of grid points are needed: a fixed Eulerian grid for the fluid flow and a moving Lagrangian grid for the fibers (Supplemental material, Figure S3). The volume force arising from the interaction of the fibers and flow is obtained by the convolution onto the Eulerian mesh of the singular forces estimated on the Lagrangian nodes; these are computed

using the fluid velocity interpolated at the location of the Lagrangian points. For each time step, the solution approach for the fibers suspended in the fluid flow is summarized as follows.

First, the fluid velocity is interpolated into the Lagrangian points by the Dirac delta function, δ [45]:

$$\mathbf{U}_{ib}(s,t) = \int_V \mathbf{u}(\mathbf{x},t)\delta(\mathbf{X}(s,t)-\mathbf{x})dV, \tag{7}$$

The fluid-solid interaction force is then calculated using the velocity difference between the fluid and solid at each Lagrangian point:

$$\mathbf{F} = \frac{\mathbf{U}-\mathbf{U}_{ib}}{\Delta t}, \tag{8}$$

where $\mathbf{U}_{ib}$ is the interpolated velocity on the Lagrangian points, $\mathbf{U}$ velocity of the Lagrangian points, ΔT the time step. The Lagrangian for $\mathbf{F}$ is then spread back to the Eulerian grid as:

$$\mathbf{f}(\mathbf{x},t) = \frac{\pi}{4{A_l}^2}\int_L \mathbf{F}(\mathbf{s},t)\delta(\mathbf{x}-\mathbf{X}(s,t))ds. \tag{9}$$

Here, $A_l = L_l/d$, is the aspect ratio of the larger-sized fiber in the bi-disperse suspension. In the next step, fiber equations are solved to find the new position of the fibers. Finally, the Navier-Stokes equations are solved to update the flow field. For the details of the numerical method, the readers are referred to our previous publication [13].

C. Short range interactions

Even though the hydrodynamic interactions are well resolved using IBM, the short-range interactions need a fine Eulerian mesh that increases computational cost. So, we use the models proposed for short range interactions to save in the computational time. The short-range interaction, $\mathbf{F}^f = \mathbf{F}^{lc} + \mathbf{F}^c + \mathbf{F}^{cons}$, is split into the lubrication correction $\mathbf{F}^{lc}$, contact force $\mathbf{F}^c$, conservative force $\mathbf{F}^{cons}$. The implementation of lubrication correction $\mathbf{F}^{lc}$ can be found in supplemental material (Supplemental material).

1. Conservative force

The conservative force can be split as $\mathbf{F}^{cons} = \mathbf{F}^A + \mathbf{F}^R$, where $\mathbf{F}^A$ is the van der Waals attractive force, and $\mathbf{F}^R$ is the repulsive force of electrostatic origin. The expressions for attractive and repulsive interactions are readily available based on previous theoretical studies and experimental data [46, 47]. The attractive force of van der Waals origin is modeled as $|\mathbf{F}^A| = F_A/(h^2+H^2)$ and acts in the normal directions toward the fibers. Here h is the inter-fiber surface separation. Moreover, H is fixed to 0.01 to prevent the divergence in $|\mathbf{F}^A|$ when $h \to 0$ (during contact). F_A controls the strength of the attraction by determining the values of the attractive force in contact. The repulsive force $\mathbf{F}^R$ also acts in the normal direction to the fibers but is opposite to the attractive force. $\mathbf{F}^R$ decays with the inter-fiber separation h over the Debye length κ as $|\mathbf{F}^R| = F_R \exp(-h/\kappa)$ [48, 49].

2. Contact force

The contact between the fibers occurs when the inter-fiber separation distance h becomes smaller than the height of surface asperity h_r as shown in figure S4, Supplemental material. Specifically, the single-asperity model of surface roughness has been widely used owing to its simplicity and effectiveness [7, 36, 50–52]. Hence, we take the same approach and model the asperity as a hemispherical bump on the fiber surface. Actual asperities might not be just hemispherical and can come in various geometries [53]. However, on average, we can model their behavior by approximately assuming them hemispherical as routinely done in the tribology literature [54]. Finally, we split the contact force $\mathbf{F}^c$ into the tangential ($\mathbf{F}_t^C$) and normal ($\mathbf{F}_n^C$) components. The normal contact force is modeled using a Hertz law, $|\mathbf{F}_n^C| = -k_n|\delta|^{3/2}$, where $\delta = h_r - h$ is the asperity deformation with h_r the asperity height, and k_n is the normal stiffness, which is a function of the fiber material properties [51, 52]. The Coulomb's friction law gives the

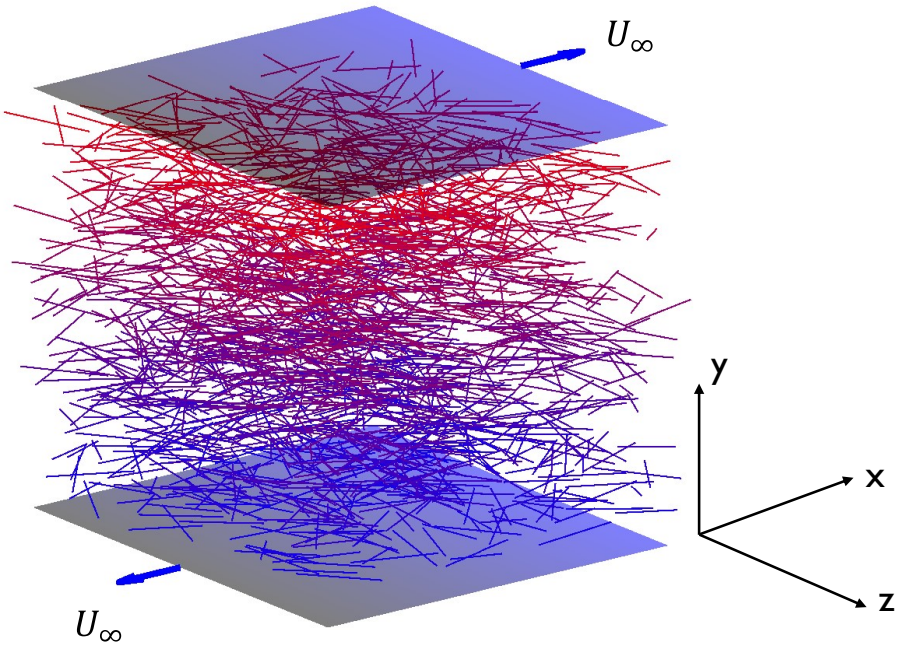

FIG. 1: Simulation setup of the shear flow of a fiber suspension. The top and bottom walls move with velocities $U_\infty = \dot{\gamma}L$ in the directions shown by the arrows.

tangential force, $|\mathbf{F}_t| = \mu|\mathbf{F}_n|$, where in the current work $\mu = 0.4$ unless otherwise stated. The typical value of μ is $0.3 - 0.5$ as measured experimentally for the polymer fibers [55, 56]. Even though little is known about the friction mechanics at the nanoscale, the Coulomb friction allows a correct prediction for flows of colloidal nanoparticles [57] or hard-sphere suspensions [50].

D. Flow configuration and domian size

To investigate the fiber suspension in a shear flow, we consider a three dimensional channel with top and bottom wall moving in opposite directions with velocity imposing a shear rate, $\dot{\gamma} = U_\infty/H$, where H is half of the channel height. At the walls, we impose no slip boundary conditions for velocities and zero gradients for the pressure. Moreover, we impose a periodic boundary condition perpendicular to the wall-normal direction. The domain size is $5 \times 8 \times 5$ in units of large fiber length in streamwise (x), wall-normal (y) and spanwise (z) directions. The number of Eulerian cells per fiber should be almost equal to the fiber's aspect ratio (L/d). For example, if the aspect ratio of the fiber is 40, 40 Eulerian grids per fiber length is required. Moreover, the number of Lagrangian points per fiber should be close to L/d to capture the dynamics of the fibers. So, first, we need to find the minimum Lagrangian points that are required for the fibers with a larger aspect ratio. The Eulerian grid spacing should be similar to Lagrangian points. The required time step to capture the fiber dynamics is $\Delta t = 10^{-4}$. The simulation setup is illustrated in Figure 1. For each case, we complete a grid and time step independency test by simulating with a bigger domain, higher grid, and time resolution, e.g., 1.5, 2, 2.5, and 3 times the current domain, grid, and time resolution, which show a negligible (less than 2 %) change in the averaged steady state suspension viscosity. We continue running the simulations until a statistically steady viscosity is observed and report the mean values after discarding the initial transients.

E. Suspension rheology

We present the rheological behavior of bi-disperse suspensions in terms of relative viscosity and first and second normal stress differences. The quantities are made dimensionless using viscous scaling. The relative viscosity is defined as:

$$\eta_r = \frac{\eta_{eff}}{\eta} \tag{10}$$

where η_{eff} is the effective viscosity of the suspension. Moreover, the relative viscosity is terms of bulk shear stress can be written as:

$$\eta_r = 1 + \Sigma^f_{xy} \tag{11}$$

where Σ^f_{xy} is time and space averaged shear stress arising from the presence of the fibers. Σ^f_{xy} is non-dimensionalized by the product of suspending fluid viscosity η and shear rate $\dot{\gamma}$. The first and second normal stress coefficients are calculated as:

$$N_1 = (\Sigma_{xx} - \Sigma_{yy})/\Sigma_{xy}, \tag{12}$$
$$N_2 = (\Sigma_{yy} - \Sigma_{zz})/\Sigma_{xy}. \tag{13}$$

We use a repulsive force magnitude as the characteristic force to scale the various forces. Consequently, the characteristics shear rate scale is $\dot{\gamma}_0 = F_R/\pi\eta d^2$, and the corresponding shear stress scale is $\sigma_0 = F_R/\pi d^2$.Therefore the dimensionless shear rate and stress can be defined as:

$$\frac{\dot{\gamma}}{\dot{\gamma}_0} = \frac{\dot{\gamma}}{F_R/\pi\eta d^2}, \tag{14}$$
$$\frac{\sigma}{\sigma_0} = \frac{\dot{\gamma}}{\dot{\gamma}_0}\Sigma_{xy} = \dot{\Gamma}\eta_r \tag{15}$$

There are three main contributions to the bulk stress: 1) the hydrodynamic contribution, Σ^h_{ij}, 2) the contact contribution, Σ^c_{ij}, and 3) the non-contact contribution, Σ^{nc}_{ij}. The computation of the total stress in the suspension including different contributions is described in the Supplemental Material.

F. Parameters

We aim to investigate the effects of dimensionless shear rate ($\dot{\gamma}/\dot{\gamma}_0$), dimensionless shear stress (σ/σ_0), volume fraction (ϕ), and bi-dispersity on the rheology of fiber suspensions. The volume fraction can be defined as:

$$\phi = \frac{\pi}{4\nu A_l^2}(N_l + N_s\frac{A_s}{A_l}) \tag{16}$$

where $\nu = V/l^3$, is the total volume of the simulation cell. N_l and N_s are the total numbers of large and small fibers in the suspension, respectively. Here A_l and A_s denote the aspect ratio of the larger and smaller-sized fiber, respectively. In addition to volume fraction, we discuss two additional parameters that are required to characterize bi-disperse suspensions as compared to mono-disperse suspensions. Although there are other options available, the following forms are typically used [34]. These are the size ratio

$$\delta = \frac{A_l}{A_s}, \tag{17}$$

and the fraction of the solid volume fraction occupied by the larger-sized fiber, defined as

$$\epsilon = \frac{\phi_l}{\phi} \tag{18}$$

TABLE II: Range of parameters explored in this study

$\dot{\gamma}/\dot{\gamma}_0$	ϕ	δ	ϵ
$0.01 - 10$	$0.02 - 0.35$	$1.61, 2.30, 3.30$	$0.0 - 1.0$

where ϕ is the bulk fiber volume fraction and ϕ_l is large-fiber volume fractions. Therefore our current system can be summarized as follows:

$$\eta_r, N_1, N_2 = f\left(\frac{\dot{\gamma}}{F_R/\pi\eta d^2}, \dot{\Gamma}\eta_r, \frac{\pi}{4\nu A_l^2}(N_l + N_s\frac{A_s}{A_l}), \frac{A_l}{A_s}, \frac{\phi_l}{\phi}\right) = f(\frac{\dot{\gamma}}{\dot{\gamma}_0}, \frac{\sigma}{\sigma_0}, \phi, \delta, \epsilon) \tag{19}$$

We simulate a shear flow by varying the dimensionless shear rate in the range $0.01 \leq \dot{\gamma}/\dot{\gamma}_0 \leq 10$, the composition in the range $0.0 \leq \epsilon \leq 1.0$. We explored three different size ratios such as $\delta = 1.61.2.30, 3.30$. We choose the size ratio, volume fraction, and composition range such that it covers the experimental measurements of the bi-disperse suspension as shown in Table I. The range of parameters numerically explored in the present work is summarized in Table II.

IV. RESULT

This section presents the results of the numerical simulations and experiments. Section IV B presents the shear rate-dependent behavior and validation of the proposed numerical model with experimental measurements. We quantify the effect of bidispersity on relative viscosity and normal stress differences in section IV C. Finally, we conclude the result section by providing the results by demonstrating the effect of volume fraction and jamming rheology. We make all the quantities dimensionless using the scaling mentioned in sections III E and III F. The suspension is simulated until a statistically steady viscosity is observed and the mean values are presented.

A. Transient rheology

The suspension is simulated until a statistically steady viscosity is observed and the mean values presented are obtained discarding the initial transients as shown in figure 2. Also, to visualize the microstructure, we display the fibers co-located with their center positioned at the origin of the axis, i.e., we shift their centers to the origin and plot fibers in the same graph as shown in Fig. 4. We calculate the average orientation of the fiber with the flow direction as shown by the solid black line. As the shear rate increases, they align more with the flow direction [Figs. 3a and 3b], eventually decreasing the hydrodynamic contributions. Moreover, the overall resistance of the suspension decreases as a result of the alignment of the fibers more with the flow direction, lowering the relative viscosity.

B. Comparison of experimental and numerical results

We start our analysis by investigating the flow of the bi-disperse fiber suspension and examining the rheological properties, considering the bidispersity in the range of $0 \leq \epsilon \leq 1$. At the limits, $\epsilon = 0$ or 1, the suspension is mono-disperse (all small or all large fibers). We demonstrate the accuracy of the proposed numerical model by directly comparing the calculated relative viscosity (η_r) and shear stress (σ/σ_0) with experimental measurements of neutrally buoyant nylon fiber suspensions, which exhibit yield stress and shear-thinning viscosity. In the experiment, the size ratio of the fibers was fixed to $\delta = 1.61$ ($\delta = \frac{l_l}{l_s} = \frac{21}{13}$), and volume fraction to $\phi = 0.10$. To get different compositions (ϵ) between 0 and 1, we vary the volume fraction of the fibers with a larger aspect ratio while maintaining a constant total volume fraction. Moreover, the fibers used in the experiment are almost rigid. The parameters chosen in our simulations mimic these experimental conditions.

The comparison between numerical simulations and experimental measurements of shear rate dependent relative viscosity and flow curves are shown in figures 4a and 4b for different compositions ϵ. The proposed computational model does an excellent job of capturing the shear thinning rheology of bi-disperse suspension of fibers. Moreover,

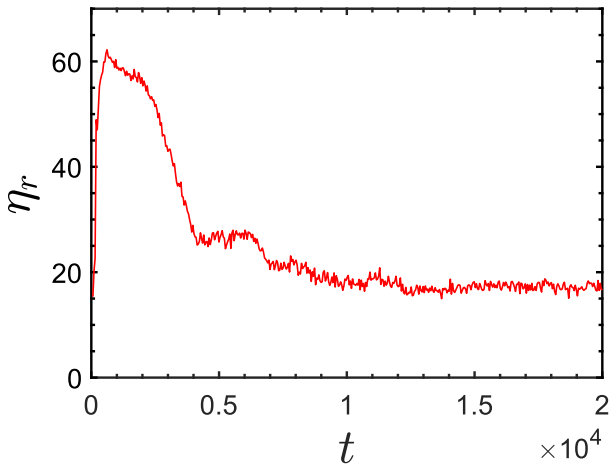

FIG. 2: Transient viscosity from the initial state to the steady state flow. The dimensionless shear rate was fixed at $\dot{\gamma}/\dot{\gamma_0} = 0.30$, composition, $\epsilon = 0.50$ and size ratio, $\delta = 1.61$.

TABLE III: Herschel–Bulkley parameters (equation 20) for different composition (ϵ) for a fixed volume fraction $\phi = 0.10$ and size ratio $\delta = 1.61$

ϵ	σ_y	a	b
0.25	0.1898	1.409	0.9975
0.50	0.8571	2.301	0.9865
1.00	2.928	7.608	0.9851

the computation flow curves in figure 4b have a rounded shape corresponding to a power law behavior at a lower dimensionless shear rate ($\dot{\gamma}/\dot{\gamma_0}$) followed by a linear segment at a high dimensionless shear rate ($\frac{\dot{\gamma}}{\dot{\gamma_0}} > 0.10$). Thus, the shear stress of nylon fiber suspensions can be described by the Herschel–Bulkley model as:

$$\frac{\sigma}{\sigma_0} = \sigma_y + a(\frac{\dot{\gamma}}{\dot{\gamma}_0})^b \tag{20}$$

where σ_y is the dimensionless yield stress obtained by fitting Eq. 20 to the computational data, a is the consistency index, and $b < 1$ is the shear thinning index. The solid lines in the flow curve (Figure 4b) demonstrate the best fit to the Herschel-Bulkley model for the computational data. The yield stress σ_y and the fitting parameters are provided in Table III. This yield stress is considered as a threshold stress required to maintain the flow defined as the dynamic yield stress [58, 59]. In the next section, we focus our attention on the effects of bi-dispersity on suspension rheology.

C. Effect of size ratio δ, and composition ϵ on rheology

1. *Relative viscosity*

As mentioned in section III F, in addition to the total volume fraction ϕ, two additional parameters, namely, the size ratio $\delta = A_l/A_s$ and composition $\epsilon = \phi_l/\phi$ determining the large-fiber fraction, are used to describe bi-disperse suspensions. In figure 5, we show the effect of bidispersity on the relative viscosity, η_r, as a function of composition ϵ for size ratios $\delta = 1.61$, 2.30, and 3.00. When varying the size ratio, we fix the aspect ratio of the smaller fibers to be 13 and vary the aspect ratio of the larger fibers to 21, 30, and 39. Moreover, to get different compositions ϵ, we vary the volume fraction of the fibers with a larger aspect ratio at a fixed total fiber volume fraction in the suspension. At the endpoints $\epsilon = 0$ and 1, the suspension is mono-disperse. However, at $\epsilon = 0$, all of the suspensions exhibit identical rheology due to size invariance. At a fixed size ratio of $\delta = 2.30$, relative viscosity increases with composition to the mono-disperse viscosity at $\epsilon = 1.0$, as depicted in figure 5. Moreover, the increase in relative viscosity is more

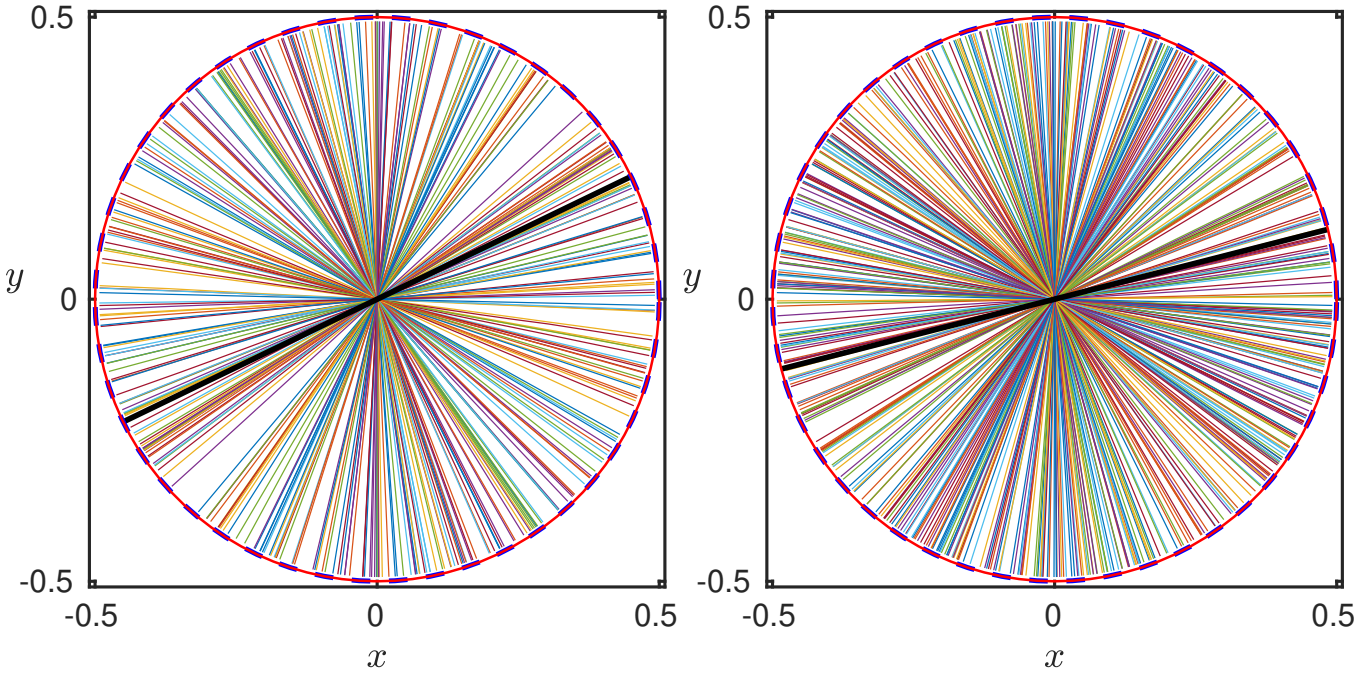

FIG. 3: Co-located filaments projected on the shear plane for dimensionless shear rate (a) $\dot{\gamma}/\dot{\gamma}_0 = 0.01$, (b) $\dot{\gamma}/\dot{\gamma}_0 = 5$. The solid black line shows the average orientation of the fibers with respect to the wall. As the shear rate increases, fibers align more with the flow direction. The solid red line represents the circles with a diameter equal to the fiber length; and the blue dashed line is the circle with a diameter equal to the mean end-to-end distance for each case. The solid red line coincides with the blue dashed line, confirming that the fibers are rigid. All simulations are performed with volume fraction $\phi = 0.17$, composition, $\epsilon = 1.0$, and size ratio, $\delta = 1.61$.

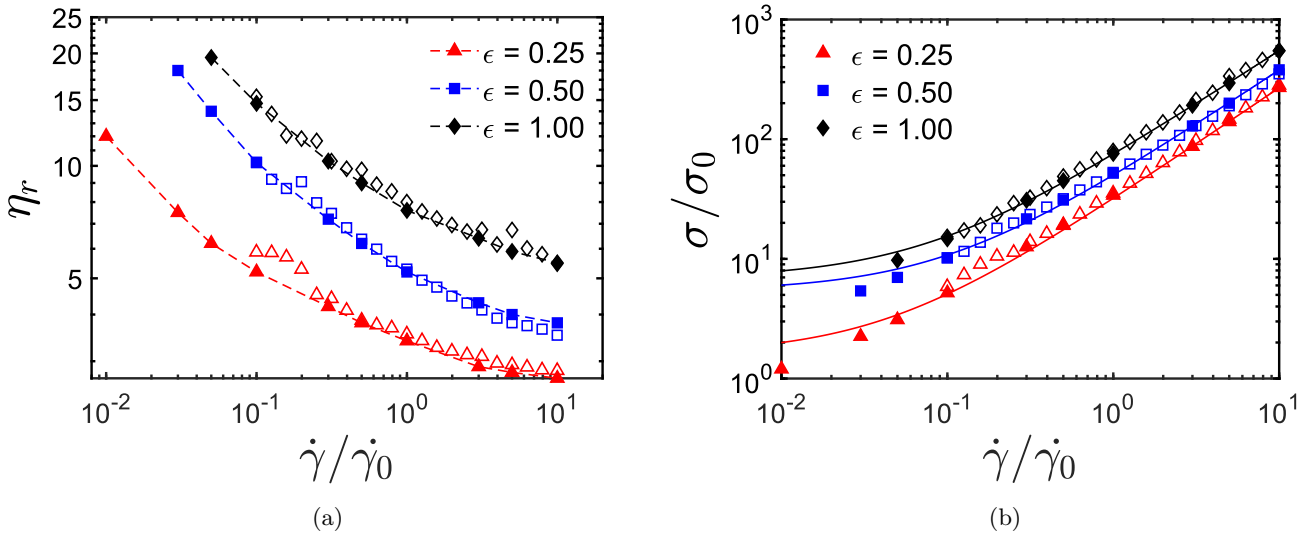

FIG. 4: The comparison of experimental and numerical values of (a) relative viscosity (η_r) and (b) shear stress ($\frac{\sigma}{\sigma_0}$) of nylon fiber suspensions at different compositions, ϵ. The hollow symbols correspond to experimental data. The solid symbols correspond to numerical data, and solid lines in the shear stress curve denote the best fit with the Herschel–Bulkley model (Eq. 20) for numerical data. Experimental shear rate and shear stress were scaled by $\dot{\gamma}_0 = 0.1$ and $\sigma_0 = 0.001$, respectively. The volume fraction was fixed to $\phi = 0.1$, and the size ratio was fixed to $\delta = 1.61$

.

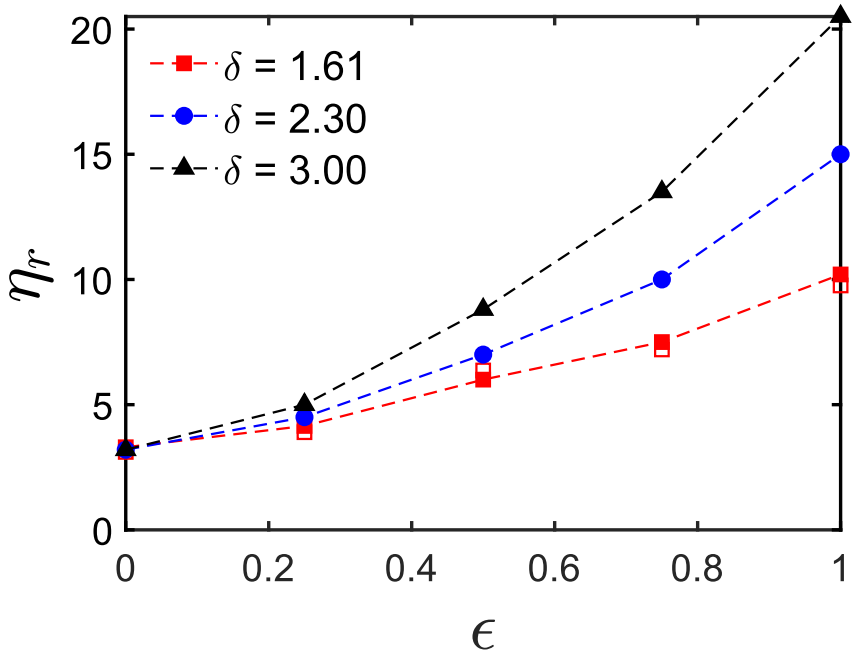

FIG. 5: Relative viscosity of bi-disperse suspensions as a function of size ratio δ, and composition $\epsilon = \phi_l/\phi$, at fixed $\phi = 0.10$. Hollow symbols correspond to experimental measurements. For all the current cases, the dimensionless shear rate was fixed at $\dot{\gamma}/\dot{\gamma}_0 = 0.5$.

pronounced at a higher size ratio ($\delta = 3.0$). To better understand the underlying mechanism of increasing viscosity with bidispersity, we separate the hydrodynamic, contact, and non-contact (attractive+repulsive) contribution to total viscosity, as shown in figure 6a and 6b. While the hydrodynamic and non-contact contributions increase weakly, the contact contribution becomes significant and dominant at a composition ϵ greater than 0.2. The length difference plays an important role in determining the contact contribution to the total viscosity of the suspension. As the aspect ratio of the fiber increases, there is a greater likelihood for increased contact between fibers on average, in comparison to smaller fibers. As the aspect ratio of the fiber increases, they can come into more contact in average compared to smaller fiber. This observation underlines the impact of contacts in the rheology of the bi-disperse fiber suspensions. Moreover, hydrodynamic, contact, and non-contact contribution to the shear stress as a function of shear rate can be found in our previous manuscript [27].

Furthermore, we focus on the orientation of the fibers in the suspension to understand the effect of bi-dispersity on the microstructure. The orbit constant $< C_b >$, when averaged over the suspending fibers, is the measure of the orientation distribution. The ratio $C/(C+1)$ is generally used to define $< C_b >$ [2, 16, 60] where,

$$C = \frac{1}{A}\tan\theta_z(\mathrm{A}^2\cos^2\theta_y + \sin^2\theta_y)^{1/2} \tag{21}$$

where θ_z is the angle of the fiber with respect to the vorticity direction (z-axis), and θ_y is the angle between the gradient direction (y-axis) and the projection of the fiber on the flow gradient (x-y) plane. If all the fibers are aligned in the flow gradient plane, the average orbit constant $< C_b >$ goes to 1. However, if the fibers are aligned with the vorticity direction (z-axis), $< C_b >$ goes to 0. We separate the orientation distribution of the larger and smaller-sized fibers, as shown in figure 7a. The orientation distribution reaches two extreme values when the suspension is mono-disperse. At $\epsilon = 0$, suspension consists of fibers with a smaller aspect ratio (A_s), and the orientation distribution reaches the maximum value, meaning that the fibers are aligning most to the flow-gradient plane. On the other hand, at $\epsilon = 1$, suspension consists of fibers with a large aspect ratio (A_l), and the orientation distribution reaches the minimum value, meaning that the fibers are deviating most from the flow gradient plane and aligning to vorticity direction (z-direction). In between the two values ($0 < \epsilon < 1$), we observe the effect of composition on the orientation of the fiber. The fibers with a lower aspect ratio A_s tend to align more with the flow direction than those with a larger aspect ratio A_l in the bi-disperse suspension as shown in figure 7a. Fibers pointing more out of the plane of shear for higher aspect

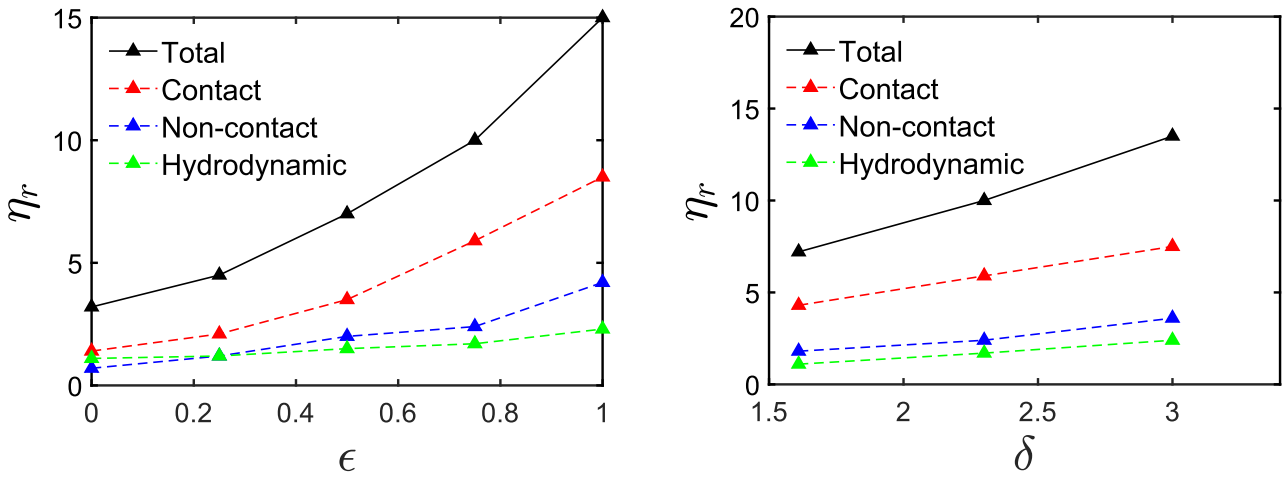

(a) (b)

FIG. 6: Total relative viscosity and contributions arising from hydrodynamic, conservative, and contact forces, as a function of (a) composition at a fixed size ratio $\delta = 2.3$, (b) size ratio at a fixed composition $\epsilon = 0.75$. At the endpoint $\epsilon = 0$ (All fibers have an aspect ratio, $A = 13$) and 1 (All fibers have an aspect ratio, $A = 30$), the suspension is mono-disperse. All the simulations were performed for a fixed dimensionless shear rate, $\dot{\gamma}/\dot{\gamma}_0 = 0.5$, and total volume fraction, $\phi = 0.10$.

ratio matches with the previous measurement [61] and numerical simulation [60, 62]. The change in fiber orientation from small to large fibers towards the vorticity direction is influenced by various factors, including hydrodynamic, contact, and non-contact interactions, as depicted in Figure 6. Adding more large fibers at a fixed volume fraction increases the hydrodynamics contribution weekly, meaning smaller fibers experience less hydrodynamic drag than large fibers. The larger hydrodynamic drag force acts to orient the large fibers more closely to the plane of the velocity gradient (x-y axis). However, for concentrated suspension $\phi = 0.10$, the significant contribution to total viscosity is coming from non-hydrodynamic interactions (attractive, repulsive, and contact interactions) (Figure 6). The interplay between these interactions determines the final orientation of the fibers. Attractive forces between fibers tend to promote ordering as they pull the fibers towards each other, which can result in a more parallel alignment of the fibers. On the other hand, repulsive forces between fibers tend to hinder ordering, as they push the fibers apart, leading to more random orientations. Our model also includes contact interaction that should hinder the alignment. Moreover, it is evident from the orientation distribution that smaller fibers exhibit a tendency to align with the plane of flow-gradient (x-y), but larger fibers demonstrate a deviation. Therefore, the alignment of the larger fibers leads to a higher level of contact when compared to the smaller fibers

Furthermore, the effect of size ratio on the orientation distribution is also shown in Figure 7b. As we mentioned earlier, to vary the size ratio of the bi-disperse suspension, we vary the aspect ratio of the larger-sized fiber (A_l), keeping the aspect ratio of the smaller-sized fiber (A_s) constant. We see that the orientation of the fibers with a smaller aspect ratio does not change significantly as the size ratio increases. However, the fibers with a larger aspect ratio tend to deviate more from the flow-gradient direction as the size ratio increases.

2. Normal stress differences

Normal stress differences are inevitable in fiber suspensions due to the presence of hydrodynamics and inter-fiber interactions [62, 63]. We present the variation of the first normal stress difference (N_1) and second normal stress difference (N_2) with bi-dispersity in figure 8. Here, we show the normal stress differences in a bi-disperse fiber suspension as a function of composition ϵ for size ratios $\delta = 1.61$, 2.30, and 3.00. The first normal stress is positive, in agreement with previous studies [20, 62, 63]. The variation of N_1 with bi-dispersity is plotted in Figure 8a. N_1 is minimum at a mono-disperse suspension of aspect ratio 13 (composition $\epsilon = 0$). The first normal stress difference increases as the composition increases and reaches the maximum value at the mono-disperse suspension of aspect ratio 39 (composition $\epsilon = 1$). A similar trend is observed for different size ratios δ. This behavior differs with the suspension of particles, where the first normal stress difference was found insensitive to bi-dispersity [34, 35]. The

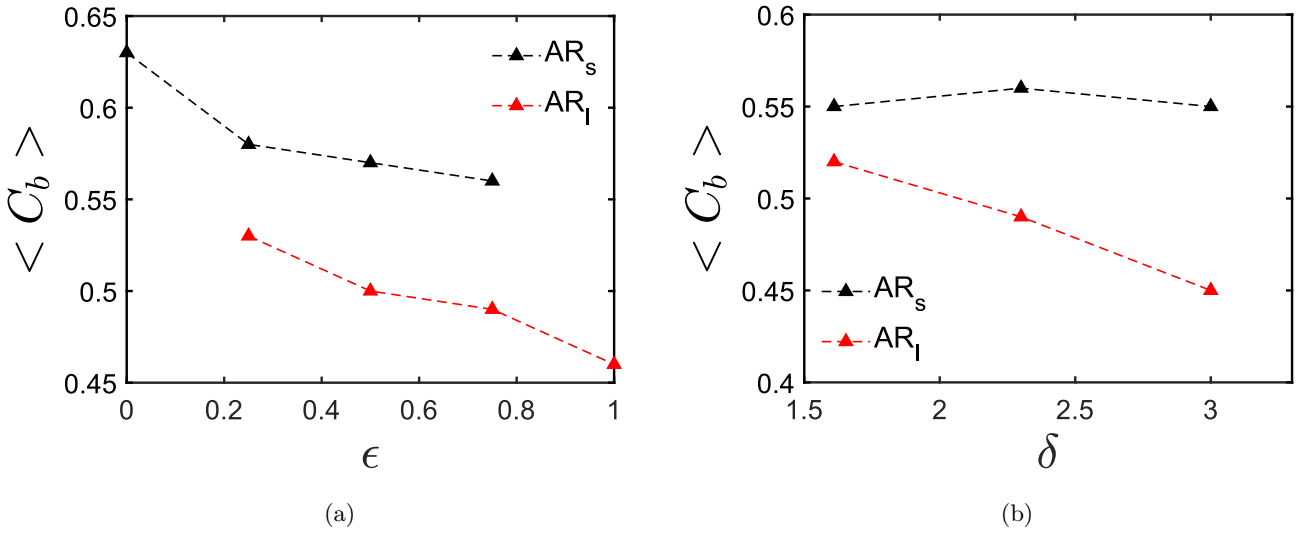

(a) (b)

FIG. 7: The mean orbit constant $< C_b >$ as a function of (a) the composition of the bi-disperse suspension for a fixed size ratio $\delta = 2.3$ and (b) size ratio of the bi-disperse suspension for a fixed composition $\epsilon = 0.75$. At the endpoint $\epsilon = 0$ (All fibers have an aspect ratio, $A = 13$) and 1 (All fibers have an aspect ratio, $A = 30$), the suspension is mono-disperse. All the simulations were performed for a fixed dimensionless shear rate, $\dot{\gamma}/\dot{\gamma}_0 = 0.5$, and total volume fraction, $\phi = 0.10$.

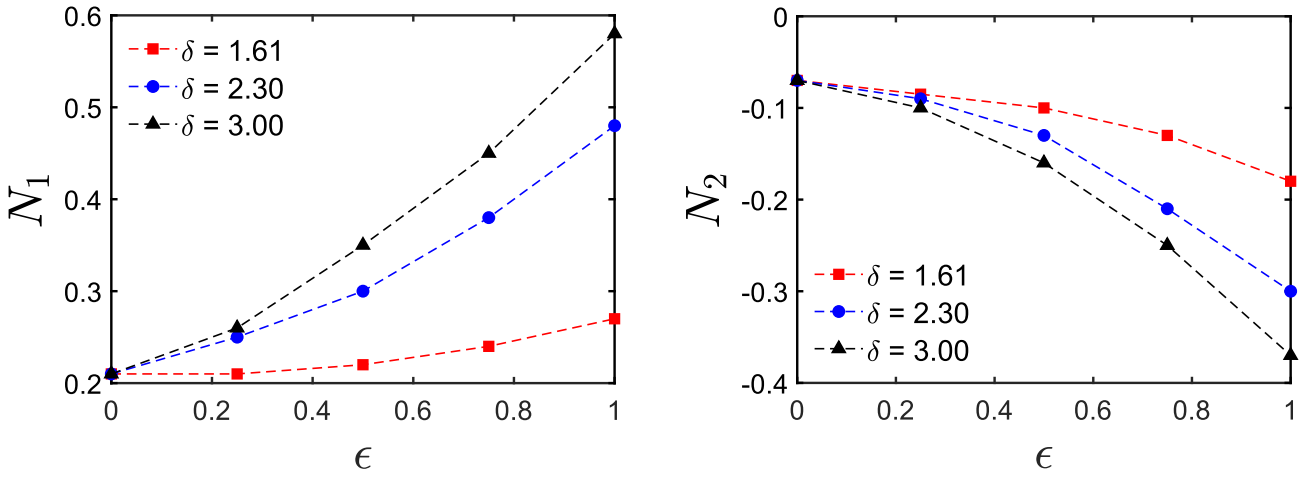

(a) (b)

FIG. 8: (a) First normal stress difference N_1 and (b) Second normal stress difference N_2 of bi-disperse suspensions as a function of composition (ϵ) for different size ratios (δ). All the simulations were performed at a fixed dimensionless shear rate $\dot{\gamma}/\dot{\gamma}_0 = 0.5$.

second normal stress difference is negative, and the magnitude is small compared to the first normal stress differences, which agrees with previous experimental studies [20, 62]. The magnitude of the second normal stress difference shows a similar trend as the first normal stress difference with bi-dispersity, hence not repeated for brevity.

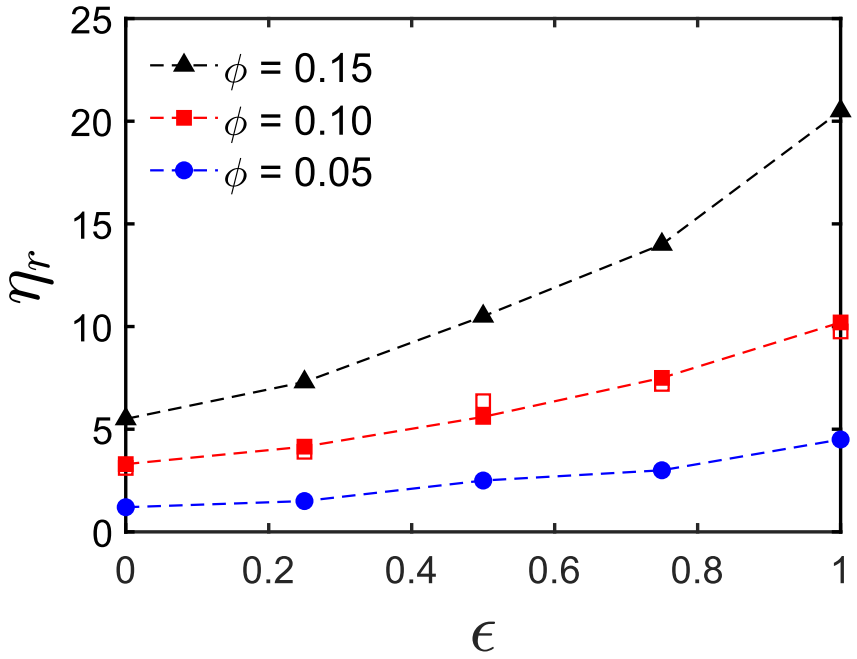

FIG. 9: Variation of relative viscosity as a function of composition ϵ, for different volume fractions. Hollow symbols correspond to experimental measurement.The size ratio was fixed to $\delta = 1.61$, and the dimensionless shear rate to $\dot{\gamma}/\dot{\gamma}_0 = 0.5$ for all the cases.

D. Bi-disperse rheology for different volume fractions

The variation of relative viscosity with bidispersity for different volume fractions is shown in figure 9. At higher volume fractions, we observe a more significant increase in relative viscosity with composition ϵ.

It is widely known that the viscosity of suspensions increases with the volume fraction of the particle phase and diverges at a specific maximum volume fraction beyond which the suspension does not flow, namely the jamming fraction ϕ_m [7, 36, 48]. In our models, fiber suspensions exhibit the same behavior. Figure 10a shows the relative viscosity η_r as a function for volume fraction ϕ for suspension compositions $0 \leq \epsilon \leq 1$, all at size ratio $\delta = 1.61$. As the viscosity increases with the composition for a fixed volume fraction (Figure 9), the viscosity diverges at a critical volume fraction ϕ_m. As shown in Figure 10a, the critical volume fraction depends on the composition of the bi-disperse suspension. Moreover, the variation of relative viscosity η_r with volume fraction ϕ can be quantified with the well known Maron-Pierce law, which has been widely applied for spherical particle suspensions [36]. Nevertheless, a modified Maron-Pierce law is required to capture the behavior of the fiber suspensions [6, 13]. Despite the availability of the Krieger-Dougerty relation [64], which has been adapted for anisotropic colloidal rods [65], we have chosen to utilize the modified Maron-Pierce law to analyze our data. This decision was based on the model's ability to effectively account for the influence of roughness, flexibility, and aspect ratio on jamming rheology, as demonstrated in our previous publications [13, 14, 27]. In our current study, as we have extended our prior model to include bi-dispersity, we have opted to retain the same modified Maron-Pierce law utilized in our previous research to maintain consistency. The following form of the Maron-Pierce law is used to fit the data in Figure 10a

$$n_r = \alpha(1 - \phi/\phi_m)^{-\beta}, \tag{22}$$

where the coefficient α, exponent β, and jamming volume fraction ϕ_m depend on the size ratio and the composition of the fiber suspension. Equation 22 does a good job of modeling the viscosity as a function of volume fraction, as seen by the solid lines in figure 10a. We discover that the relative viscosity diverges near the jamming transition with a scaling of $(\phi_m - \phi)^{-1.7}$, as opposed to $(\phi_m - \phi)^{-2}$, which is the behavior observed for a suspension of spheres [7, 36, 52]. Moreover, the scaling found here, $(\phi_m - \phi)^{-1.7}$, differs from those obtained for plastic rigid fiber suspensions, $(\phi_m - \phi)^{-0.90}$ [6]. The parameters α and ϕ_m obtained after calibrating the model with the numerical data are presented in table IV. We notice a decrease in ϕ_m from ≈ 0.36 to ≈ 0.22 with increasing composition, as shown in figure 10b.

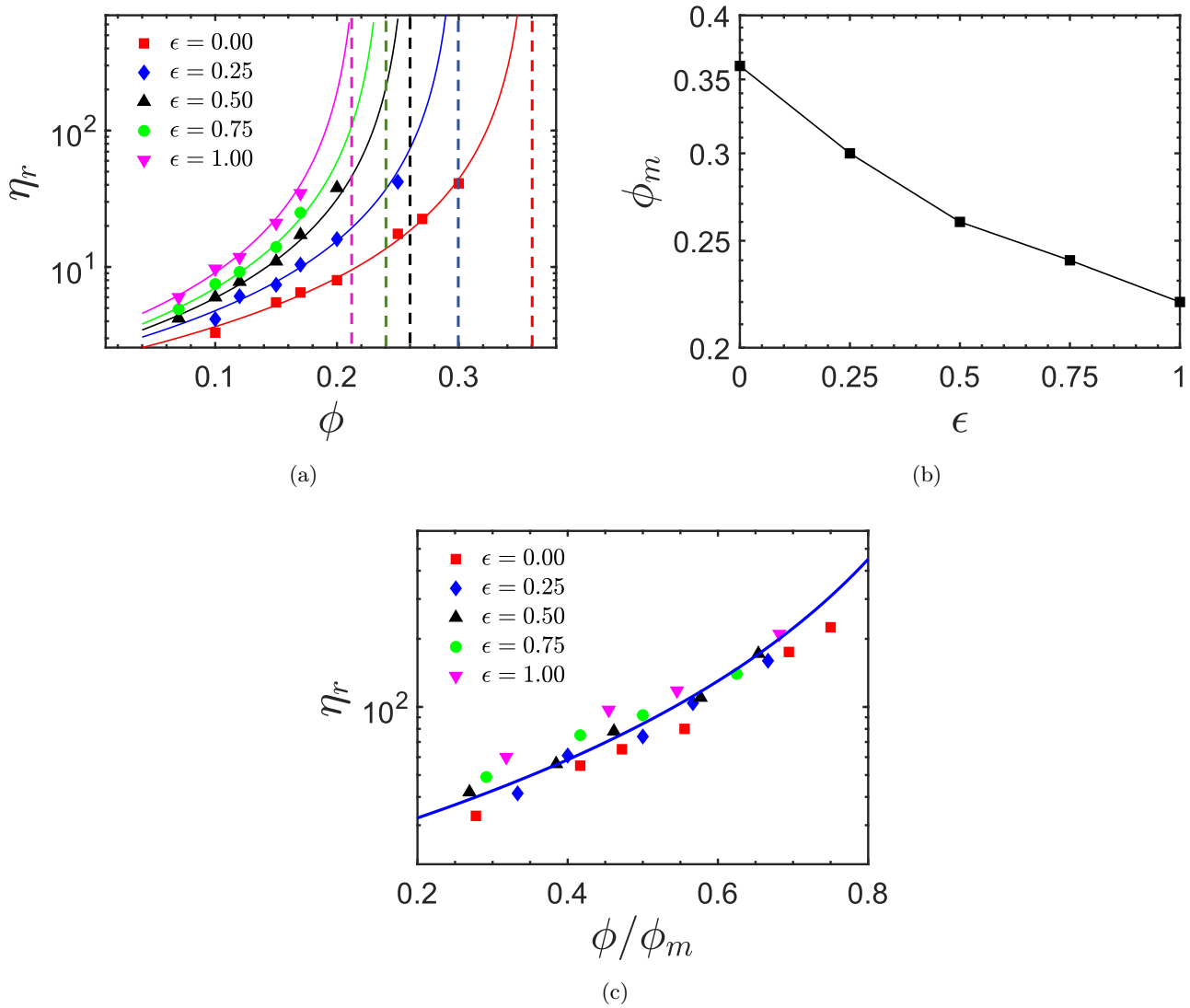

FIG. 10: (a) Relative viscosity η_r vs. volume fraction ϕ for different compositions of bi-disperse fiber suspension. Solid lines are the fitting curve with the modified Maron-Pierce law (equation 22). The vertical dashed line shows the jamming volume fraction ϕ_m for different compositions. (b) Jamming volume fraction as a function of the composition of fibers in the suspension. (c) Relative viscosity as a function of reduced volume fraction ϕ/ϕ_m for different compositions. All the simulations were performed for a fixed size ratio $\delta = 1.61$, and dimensionless shear rate $\dot{\gamma}/\dot{\gamma}_0 = 0.5$. Rescaling the volume fraction by jamming volume fraction ϕ_m leads to a collapse of the data indicating that the composition of the fiber in the bi-disperse suspension determines the jamming volume fraction once the fiber size ratio is fixed.

The maximum and minimum jamming volume fractions are observed for the mono-disperse suspension with all the fibers having aspect ratio $A = 13$ ($\epsilon = 0$) and $A = 21$ ($\epsilon = 1$), respectively. In Figure 10c, we re-plot the viscosity against the reduced volume fraction, ϕ/ϕ_m, for the data of Figure 10a, collapsing the curves for different compositions. Therefore, we can conclude that the distance from ϕ to ϕ_m determines the suspension rheology.

As increasing the size ratio leads to an increase in the relative viscosity, we would expect the jamming volume fraction to decrease as we increase the size ratio in the bi-disperse suspension. The effect of varying the size ratio for a fixed composition ($\epsilon = 0.50$) is depicted in Figure 11a. Again we employ the modified Maron-Pierce law (equation 22) to quantify the effect of size ratio on the jamming fraction ϕ_m, the coefficient α, and the exponent β. The solid lines in Figure 11a depict the fitting curve given by equation 22, while the fitting parameters are shown in table V. We find that the relative viscosity diverges near the jamming transition following $(\phi_m - \phi)^{-1.7}$, similar to the instances with various compositions previously stated. These data demonstrate that the jamming fraction reduces as the size

ϵ	ϕ_m	α
0	0.36	2.1
0.25	0.30	2.4
0.5	0.26	2.6
0.75	0.24	2.8
1.00	0.22	3.245

TABLE IV: Fitting parameters of the modified Maron-Pierce law (equation 22) for different compositions in the bi-disperse fiber suspension for a fixed size ratio $\delta = 1.61$, and dimensionless shear rate $\dot{\gamma}/\dot{\gamma_0} = 0.5$. $\beta = 1.7$ for all cases.

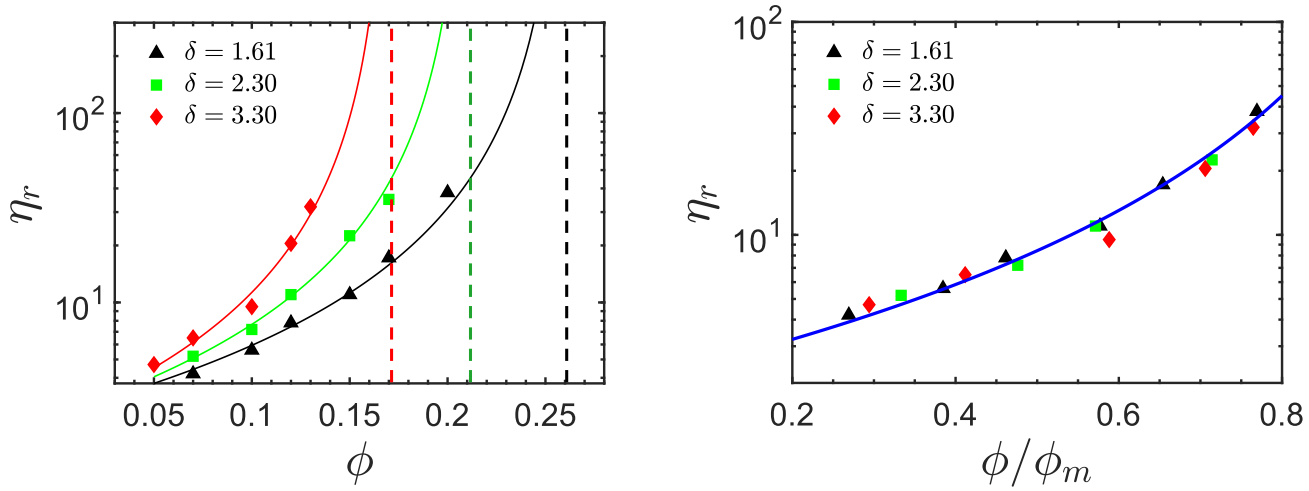

(a) (b)

FIG. 11: (a) Relative viscosity η_r vs. volume fraction ϕ for different size ratios of bi-disperse fiber suspensions. Solid lines are the fitting curve with the modified Maron-Pierce law (equation 22). The vertical dashed line shows the jamming volume fraction ϕ_m for different size ratios. (b) Relative viscosity as a function of reduced volume fraction ϕ/ϕ_m for different size ratios. All the simulations were performed for a fixed composition of $\epsilon = 0.5$ and a dimensionless shear rate $\dot{\gamma}/\dot{\gamma_0} = 0.5$. Rescaling the volume fraction by jamming volume fraction ϕ_m leads to the collapse of the data indicating that the fibers' size ratio in the bi-disperse suspension determines the jamming volume fraction once the composition is fixed.

ratio δ increases in the bi-disperse suspension. The viscosity becomes singular at lower ϕ values. These results also show how an increase in ϕ_m corresponds to a reduction in viscosity for a given ϕ. Moreover, we again re-scale the volume fraction ϕ with the jamming fraction ϕ_m, and plot them against the viscosity as shown in figure 11b. The data collapse on a single curve for different size ratios, strengthening our premise that distance from ϕ to ϕ_m determines the suspension rheology. Therefore, $\frac{\phi}{\phi_m}$ can be used as a design parameter to tune the fiber suspension's rheology

TABLE V: Fitting parameters of the modified Maron-Pierce law (equation 22) for different size ratios of the fibers in the bi-disperse suspension for a fixed composition $\epsilon = 0.50$, and dimensionless shear rate $\dot{\gamma}/\dot{\gamma_0} = 0.5$. $\beta = 1.7$ for all cases.

δ	ϕ_m	α
0	0.26	2.600
0.25	0.21	2.550
0.5	0.17	2.50

since it is easier to measure and control than size distribution and composition.

V. CONCLUSION

Bi- and poly-disperse fiber suspensions are more commonly encountered in industrial applications and natural environments than mono-disperse fiber suspensions. To promote understanding of the role of dispersity on rheology, we systematically investigate the effect of bi-dispersity for dense fiber suspensions. We conduct controlled rheological experiments with neutrally buoyant bi-disperse nylon fiber suspensions. Moreover, we perform direct numerical simulations of bi-disperse fiber suspension in a steady shear flow for a range of size ratios (δ), compositions (ϵ), and volume fractions (ϕ). We model the fibers as in-extensible one dimensional slender bodies suspended in an incompressible Newtonian fluid. The fiber dynamics is resolved using the Euler-Bernoulli beam equation, while the immersed boundary method is utilized to resolve the fluid-fiber interactions.

We begin our analysis by demonstrating the validity of the proposed model via a direct comparison between our numerical results and experimental data for bi-disperse fiber suspension. Our results show that the suspension relative viscosity η_r increases with increasing size ratio δ and composition ϵ. The increase in relative viscosity with size ratio and composition is mainly attributed to the increase of the contact-force contribution to the total stress, whereas the non-contact and hydrodynamic contributions weakly increase. Moreover, to elucidate the effect of bi-dispersity on microstructure, we present the average orientation of fiber distribution for different size ratios and compositions. The fibers with a lower aspect ratio tend to align more with the flow direction than those with a larger aspect ratio in the bi-disperse suspension. Even though the orientation of the fibers with a smaller aspect ratio does not change significantly as the size ratio increases, the fibers with a larger aspect ratio tend to deviate more from the flow-gradient direction as the size ratio increases. Moreover, the first normal stress difference increases as the composition increases and reaches the maximum value at the mono-disperse suspension of the highest aspect ratio. A similar trend is observed for different size ratios as well.

Finally, we also explore the divergence of the relative viscosity as the suspension volume fraction approaches the maximum flowable limit, i.e., the jamming fraction ϕ_m. We present a modified Maron-Pierce law to quantify the effects of bi-dispersity on ϕ_m. In particular, we show that increasing size ratio and composition decrease jamming volume fraction. Moreover, the ability shown in our previous works to obtain a collapse of mono-dispersion suspension viscosity [13, 14] when plotted against reduced volume fraction ϕ/ϕ_m extends to bi-disperse fibers suspension. This approach allows for the modeling of bi-disperse suspension viscosity using mono-disperse correlations, reducing the problem to the determination of the jamming fraction. Therefore, we can conclude that ϕ/ϕ_m can be used as a design parameter to tune the fiber suspension's rheology since it is easier to measure and control than size distribution or composition.

Accurate and rigorous experimental measurements of the rheology in poly-disperse systems continue to be lacking, with particularly few results for suspensions of fibers. Modeling the poly-disperse fiber suspension will be the immediate next step to gaining a more accurate understanding of the industrial applications of fiber suspensions. In addition, it will be an interesting study to find how the model to predict anisotropic diffusivity changes from previous studies [66] when the effect of friction is considered for numerical simulations of dense bi-disperse fiber suspension.Moreover, to get a more rigorous understanding of the effect of surface physical chemistry on bi-disperse suspension rheology, the next step would be to include a roughness model in the current numerical framework.

ACKNOWLEDGMENTS

AMA would like to acknowledge financial support from the Department of Energy via grants EE0008256 and EE0008910. RDC gratefully acknowledges support from the Lillian Gilbreth Postdoctoral Fellowship from Purdue University College of Engineering.

[1] E. Lauga and T. R. Powers, *Reports on progress in physics*, 2009, **72**, 096601.
[2] S. B. Lindström and T. Uesaka, *The Journal of chemical physics*, 2008, **128**, 024901.
[3] F. Lundell, L. D. Söderberg and P. H. Alfredsson, *Annual Review of Fluid Mechanics*, 2011, **43**, 195–217.
[4] M. Hassanpour, P. Shafigh and H. B. Mahmud, *Construction and Building Materials*, 2012, **37**, 452–461.
[5] R. Elgaddafi, R. Ahmed, M. George and F. Growcock, *Journal of Petroleum Science and Engineering*, 2012, **84**, 20–28.
[6] F. Tapia, S. Shaikh, J. E. Butler, O. Pouliquen and É. Guazzelli, *Journal of Fluid Mechanics*, 2017, **827**, R5.

[7] R. More and A. Ardekani, *Journal of Rheology*, 2020, **64**, 283–297.
[8] J. Mewis and A. Metzner, *Journal of Fluid Mechanics*, 1974, **62**, 593–600.
[9] N. J. Wagner and J. F. Brady, *Physics Today*, 2009, **62**, 27–32.
[10] M. M. Denn and J. F. Morris, *Annual review of chemical and biomolecular engineering*, 2014, **5**, 203–228.
[11] O. Du Roure, A. Lindner, E. N. Nazockdast and M. J. Shelley, *Annual Review of Fluid Mechanics*, 2019, **51**, 539–572.
[12] M. Boodaghidizaji, M. Khan and A. M. Ardekani, *Physics of Fluids*, 2022, **34**, 053101.
[13] M. Khan, R. V. More, A. A. Banaei, L. Brandt and A. M. Ardekani, *Physical Review Fluids*, 2023, **8**, 044301.
[14] M. Khan, R. V. More and A. M. Ardekani, *Physics of Fluids*, 2023, **35**, 013337.
[15] J. Wu and C. K. Aidun, *International Journal of Multiphase Flow*, 2010, **36**, 202–209.
[16] J. Wu and C. K. Aidun, *Journal of fluid mechanics*, 2010, **662**, 123–133.
[17] A. A. Banaei, M. E. Rosti and L. Brandt, *Journal of Fluid Mechanics*, 2020, **882**, A5.
[18] S. B. Lindström and T. Uesaka, *Physics of fluids*, 2007, **19**, 113307.
[19] S. Bounoua, E. Lemaire, J. Férec, G. Ausias, A. Zubarev and P. Kuzhir, *Journal of Fluid Mechanics*, 2016, **802**, 611–633.
[20] S. Bounoua, P. Kuzhir and E. Lemaire, *Journal of rheology*, 2016, **60**, 661–671.
[21] S. Bounoua, E. Lemaire, J. Férec, G. Ausias and P. Kuzhir, *Journal of Rheology*, 2016, **60**, 1279–1300.
[22] G. B. Jeffery, *Proceedings of the Royal Society of London. Series A, Containing papers of a mathematical and physical character*, 1922, **102**, 161–179.
[23] E. Hinch and L. Leal, *Journal of Fluid Mechanics*, 1973, **57**, 753–767.
[24] M. A. Bibbó, *PhD thesis*, Massachusetts Institute of Technology, 1987.
[25] E. Anczurowski, R. Cox and S. Mason, *Journal of Colloid and Interface Science*, 1967, **23**, 547–562.
[26] A. Okagawa and S. Mason, *Journal of Colloid and Interface Science*, 1973, **45**, 330–358.
[27] M. Khan, R. V. More, L. Brandt and A. M. Ardekani, *Physical Review Fluids*, 2023, **8**, 064306.
[28] C. Lang and M. P. Lettinga, *Macromolecules*, 2020, **53**, 2662–2668.
[29] G. Marrucci and N. Grizzuti, *Journal of Polymer Science: Polymer Letters Edition*, 1983, **21**, 83–86.
[30] G. Marrucci and N. Grizzuti, *Journal of non-newtonian fluid mechanics*, 1984, **14**, 103–119.
[31] M. Doi and S. Edwards, *Journal of the Chemical Society, Faraday Transactions 2: Molecular and Chemical Physics*, 1978, **74**, 560–570.
[32] M. Doi, S. F. Edwards and S. F. Edwards, *The theory of polymer dynamics*, oxford university press, 1988, vol. 73.
[33] R. Larson and D. Mead, *Journal of Polymer Science Part B: Polymer Physics*, 1991, **29**, 1271–1285.
[34] S. Pednekar, J. Chun and J. F. Morris, *Journal of Rheology*, 2018, **62**, 513–526.
[35] C. Gamonpilas, J. F. Morris and M. M. Denn, *Journal of Rheology*, 2016, **60**, 289–296.
[36] R. More and A. Ardekani, *Journal of Rheology*, 2020, **64**, 1107–1120.
[37] N.-S. Cheng, *Industrial & engineering chemistry research*, 2008, **47**, 3285–3288.
[38] A. Volk and C. J. Kähler, *Experiments in Fluids*, 2018, **59**, 75.
[39] R. Szeto, J. C. Overton, A. C. Dos Santos, C. Eby, N. S. Mosier, E. Ximenes, M. R. Ladisch and K. A. Erk, *Biotechnology Progress*, 2021, **37**, e3216.
[40] L. A. Segel and G. H. Handelman, *Mathematics applied to continuum mechanics*, SIAM, 2007.
[41] W.-X. Huang, S. J. Shin and H. J. Sung, *Journal of computational physics*, 2007, **226**, 2206–2228.
[42] A. Pinelli, M. Omidyeganeh, C. Brücker, A. Revell, A. Sarkar and E. Alinovi, *Meccanica*, 2017, **52**, 1503–1514.
[43] H. K. Versteeg and W. Malalasekera, *An introduction to computational fluid dynamics: the finite volume method*, Pearson education, 2007.
[44] A. J. Chorin, *Mathematics of computation*, 1968, **22**, 745–762.
[45] A. M. Roma, C. S. Peskin and M. J. Berger, *Journal of computational physics*, 1999, **153**, 509–534.
[46] L. Bergström, *Colloids and Surfaces A: Physicochemical and Engineering Aspects*, 1998, **133**, 151–155.
[47] J. N. Israelachvili, *Intermolecular and surface forces*, Academic press, 2011.
[48] A. Singh, S. Pednekar, J. Chun, M. M. Denn and J. F. Morris, *Physical review letters*, 2019, **122**, 098004.
[49] R. V. More and A. M. Ardekani, *arXiv preprint arXiv:2011.07038*, 2020.
[50] S. Gallier, E. Lemaire, F. Peters and L. Lobry, *Journal of Fluid Mechanics*, 2014, **757**, 514–549.
[51] L. Lobry, E. Lemaire, F. Blanc, S. Gallier and F. Peters, *Journal of Fluid Mechanics*, 2019, **860**, 682–710.
[52] R. V. More and A. M. Ardekani, *Journal of Rheology*, 2020, **64**, 67–80.
[53] R. I. Tanner and S. Dai, *Journal of Rheology*, 2016, **60**, 809–818.
[54] C. P. Broedersz and F. C. MacKintosh, *Reviews of Modern Physics*, 2014, **86**, 995.
[55] F. P. Bowden and D. Tabor, *The Friction and Lubrication of Solids-Part II.*, Oxford, England, University Press, 1964.
[56] M. P. Petrich and D. L. Koch, *Physics of Fluids*, 1998, **10**, 2111–2113.
[57] M. Fujita and Y. Yamaguchi, *Physical Review E*, 2008, **77**, 026706.
[58] P. Moller, A. Fall, V. Chikkadi, D. Derks and D. Bonn, *Philosophical Transactions of the Royal Society A: Mathematical, Physical and Engineering Sciences*, 2009, **367**, 5139–5155.
[59] N. J. Balmforth, I. A. Frigaard and G. Ovarlez, *Annual review of fluid mechanics*, 2014, **46**, 121–146.
[60] B. Snook, J. E. Butler and É. Guazzelli, *Journal of Fluid Mechanics*, 2016, **786**, 128–153.
[61] M. P. Petrich, D. L. Koch and C. Cohen, *Journal of non-newtonian fluid mechanics*, 2000, **95**, 101–133.
[62] B. Snook, L. M. Davidson, J. E. Butler, O. Pouliquen and E. Guazzelli, *Journal of fluid mechanics*, 2014, **758**, 486.
[63] M. Keshtkar, M. Heuzey and P. Carreau, *Journal of Rheology*, 2009, **53**, 631–650.
[64] I. M. Krieger and T. J. Dougherty, *Transactions of the Society of Rheology*, 1959, **3**, 137–152.

[65] N. M. James, H. Xue, M. Goyal and H. M. Jaeger, *Soft matter*, 2019, **15**, 3649–3654.
[66] A. Salahuddin, J. Wu and C. Aidun, *Journal of fluid mechanics*, 2012, **692**, 153–182.